# $CO_2$ Foaming in Thin Films of Block Copolymer Containing Fluorinated Blocks

**Lei Li,[†] Taichi Nemoto,[‡] Kenji Sugiyama,[‡] and Hideaki Yokoyama*,[†]**

*Nanotechnology Research Institute, National Institute of Advanced Industrial Science and Technology, 1-1-1, Higashi, Tsukuba, Ibaraki 305-8565, Japan, and Department of Organic and Polymeric Materials, Graduate School of Science and Engineering, Tokyo Institute of Technology, Ookayama, Meguro-Ku, Tokyo 152-8552, Japan*

*Received February 13, 2006; Revised Manuscript Received May 1, 2006*

ABSTRACT: A fabricating method of nanocellular structures in single-layer polymeric thin films was developed using supercritical carbon dioxide and fluorinated copolymer templates as reported in our previous communication [Li, L.; Yokoyama, H.; Nemoto, T.; Sugiyama, K. *Adv. Mater*. **2004**, *16*, 1226−1229]. This paper presents the details of the fabrication of nanocellular thin films. The morphology in the as-cast films depends on the solvent casting process and plays an important role for the final structures after the following the $scCO_2$ process. However, the nanocellular structures are not simply templated from the nanodomains; reconstruction of the structures during the $CO_2$ processes is not negligible. The number density of nanocells is significantly smaller than that of PFMA nanodomains before the $CO_2$ process. Starting from spherical domains followed by an $scCO_2$ process at a pressure from 8 to 20 MPa, nanocells appear with an average diameter ranging from 15 to 30 nm. SEM cross-sectional views in addition to in-plane views of the nanocellular thin films prove that not open porous but closed cellular structures are formed in films irrespective of thickness. Such nanocellular formation is primarily due to swelling of PFMA domains followed by gentle removal of $CO_2$ at reduced temperature, but expansion on depressurization still influences the size and its distribution. The size distribution of cells is effectively reduced either by lowering depressurization temperature or by adding a low molecular weight homopolymer.

## Introduction

Nanoporous materials represent a new class of materials that have attracted both industrial and academic interests. In past years, nanoporous materials have been widely investigated for a variety of applications such as molecular and protein separation, catalysis, and ultralow dielectric devices.[1−4] Recently, block copolymers have been receiving an increasing attention as a candidate for an ideal template of nanostructured materials due to their registered self-assembly.[5,6] They provide an access to nanoscale structures, typically 5−30 nm, that are not easily accessible for traditional methods. One of the successful examples is the ordered nanoporous polymeric materials fabricated from an ordered block copolymer precursor by Lee et al.[7,8] In their pioneering work, triblock copolymer thin films of poly(4-vinylphenyldimethyl-2-propoxysilane)-*b*-polyisoprene-poly(4-vinylphenyldimethyl-2-propoxysilane) were exposed with ozone to remove the cylindrical polyisoprene domains. The resultant nanoporous films have a pore size of 25 nm and surface area of 50 $m^2/g$. Many techniques have been developed to control the shape and size of nanoporous materials on the same basis.[9−15] The essential part of the methodology is that minority domains are selectively removed by chemicals, heat, ozone, or UV. However, strong oxidation or high temperature may limit the applicability of the process. Full degradation of a macroscopic sample can be difficult to be achieved when the original structure is a discrete spherical domain structure, from which there are no paths for the decomposed fragments escaping. Such decomposed fragments may remain in the materials and cause secondary contamination. A nondestructive process without residue is more desired in both scientific and practical viewpoints.

The potential benefits of using supercritical carbon dioxide ($scCO_2$) for a variety of applications have been realized, including synthesis, processing, and structure control of materials.[16] The high diffusivity, low interfacial tension, and excellent surface wettability of $scCO_2$ allow us to address many problems associated with microelectronics industry.[17] In addition, $scCO_2$ is an environmentally benign medium and readily recyclable. $scCO_2$ has already been recognized as a porogenic solvent to introduce pores of various size in polymeric materials by tuning process conditions.[18−20] In our recent research,[21,22] it was further found that the nanoscale cells (nanocells), closed cells of the order of 10−30 nm, could be produced within the nanodomains of $CO_2$-philic PFMA blocks of polystyrene-*b*-poly(perfluorooctylethyl methacrylate) (PS−PFMA) using the $scCO_2$ process. In our method, the $CO_2$-philic PFMA block domains work as a template to localize and stabilize the $scCO_2$ droplets thanks to the high affinity of the fluorinated block to $scCO_2$. In the following temperature quench, the surrounding PS matrix becomes glassy and fixes the structure while a significant amount of $CO_2$ still remains in the PFMA domains. After depressurization, empty nanocells are formed in the PFMA domains with the skeleton of the PS domain. This methodology apparently provides closed nanocellular structures that are difficult for the decomposing strategy to access as mentioned earlier. However, there still exist some suspended questions in our previous communications.[21,22] The objective of this report is to show the comprehensive results of nanocellular formation in thin films and discuss the mechanism of nanocellular forming.

## Experimental Section

**Polymer Synthesis and Sample Preparation.** Polystyrene-*b*-poly(perfluorooctylethyl methacrylate) (PS−PFMA) was synthe-

---

[†] National Institute of Advanced Industrial Science and Technology.
[‡] Tokyo Institute of Technology.
* To whom correspondence should be addressed. E-mail: yokoyama@ni.aist.go.jp.

10.1021/ma060325l CCC: \$33.50 © 2006 American Chemical Society
Published on Web 06/09/2006

sized by sequential anionic polymerization of styrene and perfluorooctyl methacrylate in tetrahydrofuran at −78 °C. The molecular weights of PS and PFMA blocks are 20 000 and 13 000 g mol$^{-1}$, respectively. The details of the polymerization and characterization of the PS−PFMA block copolymer have been described elsewhere.[23] The silicon wafers were used as received. The PS−PFMA copolymer was dissolved either in a mixture of toluene (Wako) and 1,1,1,3,3,3-hexafluoro-2-propanol (Wako) (80/20 by weight) or in α,α,α-trifluorotoluene (Aldrich). The films were prepared by spin-casting the solution on Si substrates. Film thickness was controlled by concentration of the solutions and rotating speed.

**scCO$_2$ Process.** A stainless steel high-pressure vessel for CO$_2$ processes was connected to a high-pressure liquid chromatography pump (JASCO PU-2086 plus) with a cooling head and to a back-pressure regulator (JASCO SCF-Bpg). Films of PS−PFMA were placed in the high-pressure vessel at 60 °C for 1 h with a constant pressure. The vessel was placed in an ice bath to quench the films to 0 °C while maintaining the pressure using the pump and regulator. After the temperature and pressure were stabilized, pressure was released. The depressurization rate was controlled at 0.5 MPa/min.

**Characterization of Film Surface and Nanocells.** Film thickness and refractive index were measured with a JASCO M-220 ellipsometer with incident light in a wavelength range of 400−800 nm at an incident angle of 60° with respect to the surface normal. The etching process to expose embedded cellular structures to the surface was performed with a reactive ion etcher (SAMCO compact etcher FA-1) with a CF$_4$ flow rate of 2 mL/min, a pressure of 10 Pa, and a power density of 10 W/cm$^2$. Under this condition, the etching rate for PS−PFMA copolymer thin films is ∼1 nm/s. The surface topography due to the embedded cell structures revealed by RIE was characterized by atomic force microscopy (AFM) and scanning electronic microscopy (SEM). AFM measurements were carried out in the tapping mode with a Seiko Instruments SPA300HV. We used silicon tips with a spring constant of 22 N/m. SEM images were obtained using an environmental scanning electron microscope (ESEM) (Philips XL20 ESEM-FEG) equipped with a field-emission gun under high-vacuum conditions. A 10 keV electron beam was used for the observation. No conductive coatings were applied onto the specimen surfaces.

## Results and Discussion

**Domain Structures in As-Cast Films.** A PS−PFMA thin film with a thickness of 47 nm, named PS−PFMA47, was spun-cast from a mixture of toluene (80 wt %) and 1,1,1,3,3,3-hexafluoro-2-propanol (HFP) (20 wt %). Although the weight fraction of fluorinated block is 39% (29% in volume), which is likely to lead to a cylindrical domain structure, spherical PFMA nanodomains are found as in Figure 1a after the top layer of film was removed by reactive ion etching (RIE) with CF$_4$ gas under the conditions described in the Experimental Section. Many kinds of active species have been detected in CF$_4$ plasma,[24] such as radicals (e.g., CF$_3$, CF$_2$, CF), atoms (e.g., F, O), and ions (e.g., CF$_3^+$, CF$_3^-$, and F$^-$). Such atoms and radicals can decompose a polymer in distinct ways including random chain scission and decomposition of side group from the material surface with a controlled rate.[25] PS is a vinyl-type polymer (relatively insensitive positive resist), while PFMA is a vinylidene-type polymer (efficient negative resist). Appearing topological pattern on the surface after RIE is attributed to the higher etching rate for PFMA. The top layer is spontaneously covered by PFMA blocks so that no topological features are found on the surface. When the etching front reaches the embedded spherical PFMA nanodomains in PS matrix, the height difference between PS and PFMA domains is detected by AFM. It should be noted that CF$_4$ RIE makes dimples with a depth of 3−4 nm, which can be easily distinguished from nanocellular structures that will be discussed later. The dimple pattern with a small amplitude in the topographic image appearing after reactive ion etching in Figure 1a is not embedded porous cellular structures but the PFMA domains. The spherical shape of the nanodomains does not change even after long thermal annealing as shown in Figure 1b; the size and spacing of spherical domains, however, increase. The number density of PFMA nanodomains is plotted against annealing time in Figure 1c. It is found that the number density of PFMA nanodomains decreases from 14.8 × 10$^{10}$ to 8.3 × 10$^{10}$ cm$^{-2}$ after 60 h thermal annealing at 130 °C. Since the total mass of the copolymer on the substrate is fixed, the decreasing number density must balance with the increasing aggregation number. The average diameter of the PFMA domains grows from 10.7 nm in the as-cast film to 15.5 nm after 60 h annealing, as shown in Figure 1b. Even after annealing 60 h at 130 °C, the number density does not seem to reach the equilibrium. Long-range order is also lost in the film. The primary reason for this slow reconstruction of sphere size and poor long-range order is the strong interaction between PS and PFMA. To change number density, block copolymer chains must diffuse by hopping, which is reduced exponentially by the segregation strength.[26,27] Equilibration of aggregation number is even slower than the rate expected from the diffusion coefficient (hopping rate).[28] Under such reduced mobility, the initial morphology tends to be stuck in a metastable state. Complete shape transformation, e.g., sphere to cylinder, by thermal annealing may not be possible in an experimental time scale. The use of α,α,α-trifluorotoluene as spin-casting solvent completely changes the morphology formed in as-cast films. Morphologies in the as-cast and annealed films are shown in parts d and e of Figure 1, respectively. By selecting a solvent selective to the fluorinated block, cylindrical fluorinated domains are formed in the as-cast film. Even after 60 h annealing, this block copolymer does not reach the equilibrium morphology. Throughout this study, we used a mixed solvents of toluene and HFP to start the nanocellular process from spherical PFMA domains.

**Formation of Nanocells by the CO$_2$ Process.** We processed a PS−PFMA thin film of a thickness of 51 nm on a silicon wafer with 15 MPa CO$_2$ pressure for 1 h and slowly depressurized as described in the Experimental Section. AFM and SEM were employed to observe the nanostructures in copolymer thin films. However, neither AFM nor SEM finds nanostructures on the film surface after the CO$_2$ process. RIE has been proved to etch polymer films layer by layer under a controlled etching rate without destroying morphologies.[29,30] RIE with CF$_4$ gas was employed under the conditions described in the Experimental Section. The etching rate under the condition is ∼1 nm/s. A series of AFM images in the sequence of etched thickness (etching time) are shown in Figure 2. No special features are found either on the surface of the film after the CO$_2$ process (a) or on the surface of the film after 10 nm etching (b). The blurred featureless surfaces indicate the absence of nanocells in the depth down to 10 nm. After 13 nm etching, however, dimples start to appear sporadically (c). An increasing number of cells appear at the freshly exposed surface as etching process proceeds. After 15 nm of etching, the number density of the visible cells reaches a maximum (d), and the apparent diameter of dimples increases with further etching down to 20 nm (e). Further etching down to 40 nm, i.e., 11 nm thick film remaining, destroys the cell structure (f). Although the average etching rate for the cellular films is faster than that for dense copolymer films due to voids, the etching rate for the top covering layer of the nanocellular structures should be the same as that for dense films until the dimples start to appear. From the sequence

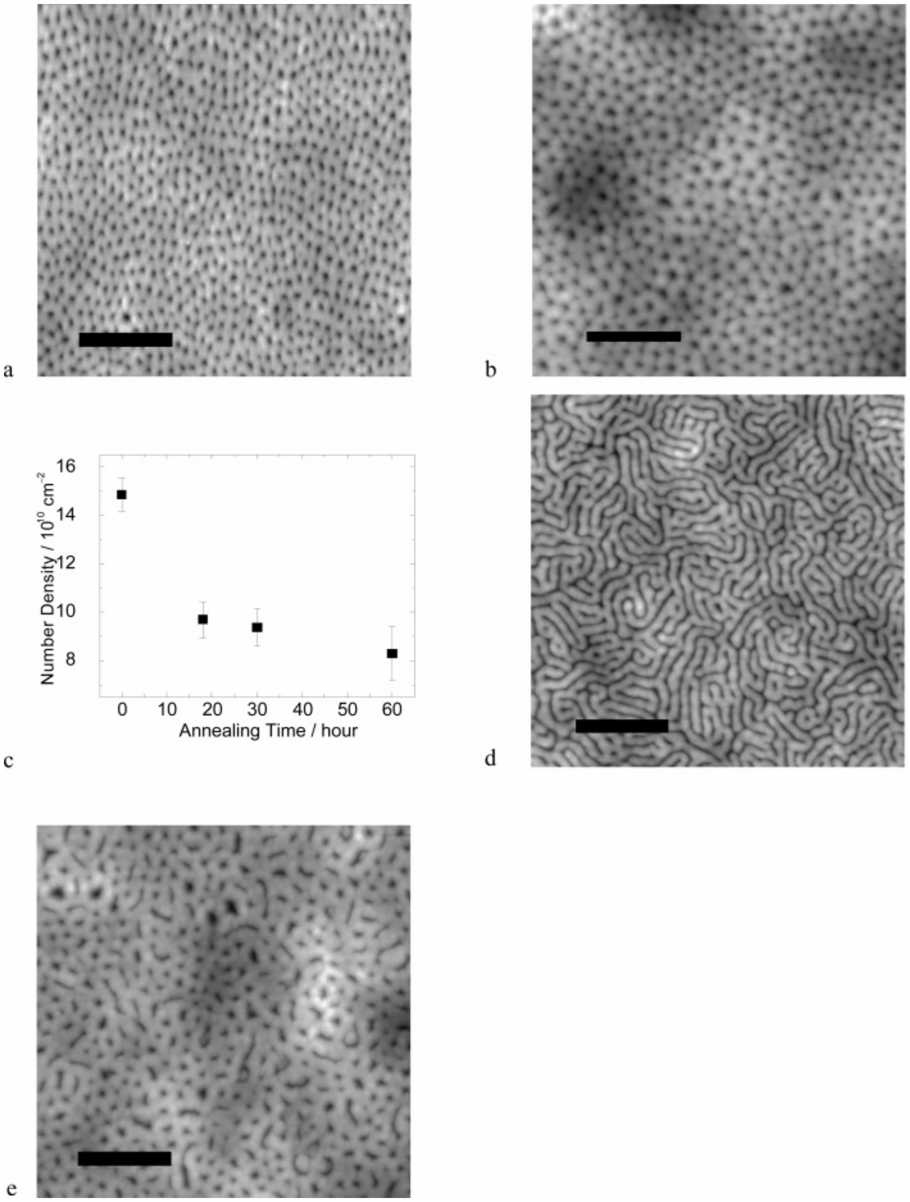

**Figure 1.** Topographic images of PS−PFMA thin films spun-cast using the mixed solvents (a) and subsequent thermal annealing at 130 °C for 60 h (b). Darker PFMA domains are found in PS matrix due to selective etching of PFMA by RIE. The annealing time dependence of the number density of PFMA nanodomains is plotted in panel (c). Topographic images of PS−PFMA thin films spun-cast using α,α,α-trifluorotoluene (d) and subsequent thermal annealing at 130 °C for 60 h (e). The bars indicate 200 nm.

of images, we can estimate the thickness of the surface skin layer. The film surface is covered with 15 nm of skin layer, and the center of the cells is located at ∼20 nm from the film surface. In conventional $CO_2$-foaming, skin layer thickness is determined by the balance of evaporation of $CO_2$ from the film surface and foaming in bulk. A typical thickness of such a skin layer is on the order of a micron. The skin layer is a few orders of magnitude thinner than conventional skin layers. It has been reported that the surface of block copolymers with fluorinated block is fully covered by the fluorinated blocks to reduce the total free energy of the system by exposing the lower surface energy fluorinated blocks.[31,32] Such a surface segregation layer grows even thicker at the $CO_2$ interface than at the vacuum interface (surface) due to the affinity of fluorinated blocks to $CO_2$.[33] In such a segregated planar layer of PFMA, foaming of $CO_2$ is not possible, and thus the skin layer of a thickness of ca. 15 nm forms.

Four pieces of PS−PFMA47 thin films were processed with $scCO_2$ according to the procedure mentioned in the Experimental Section at saturation pressures of 8, 10, 15, and 20 MPa. The topographic images of nanocells at different saturation pressures are shown in Figure 3a−d. The images are the surface topologies after removal of the surface layer by RIE. The corresponding SEM images of nanocells are shown in Figure 3e−h. Since the electron density contrast between PS and PFMA is too weak to be distinguishable in the secondary electron images, those SEM images do not represent the domain structures of PFMA but the topological dimple structures produced by the $scCO_2$ process and subsequent etching process. It should be pointed out that the depth of dimples on the surfaces in Figures 2 and 3 is more than 15 nm, which is much larger than that of PFMA nanodomains of as-cast and annealed films, i.e. 4 nm deep dimples, caused by etching rate mismatch as shown in Figure 1. As saturation pressure increases, the size of cells increases. The trend is observed either in the AFM or SEM image. Although the opening of cells after etching varies depending on etching time as shown in Figure 2, we selected the right etching time to maximize the apparent diameter of opening so

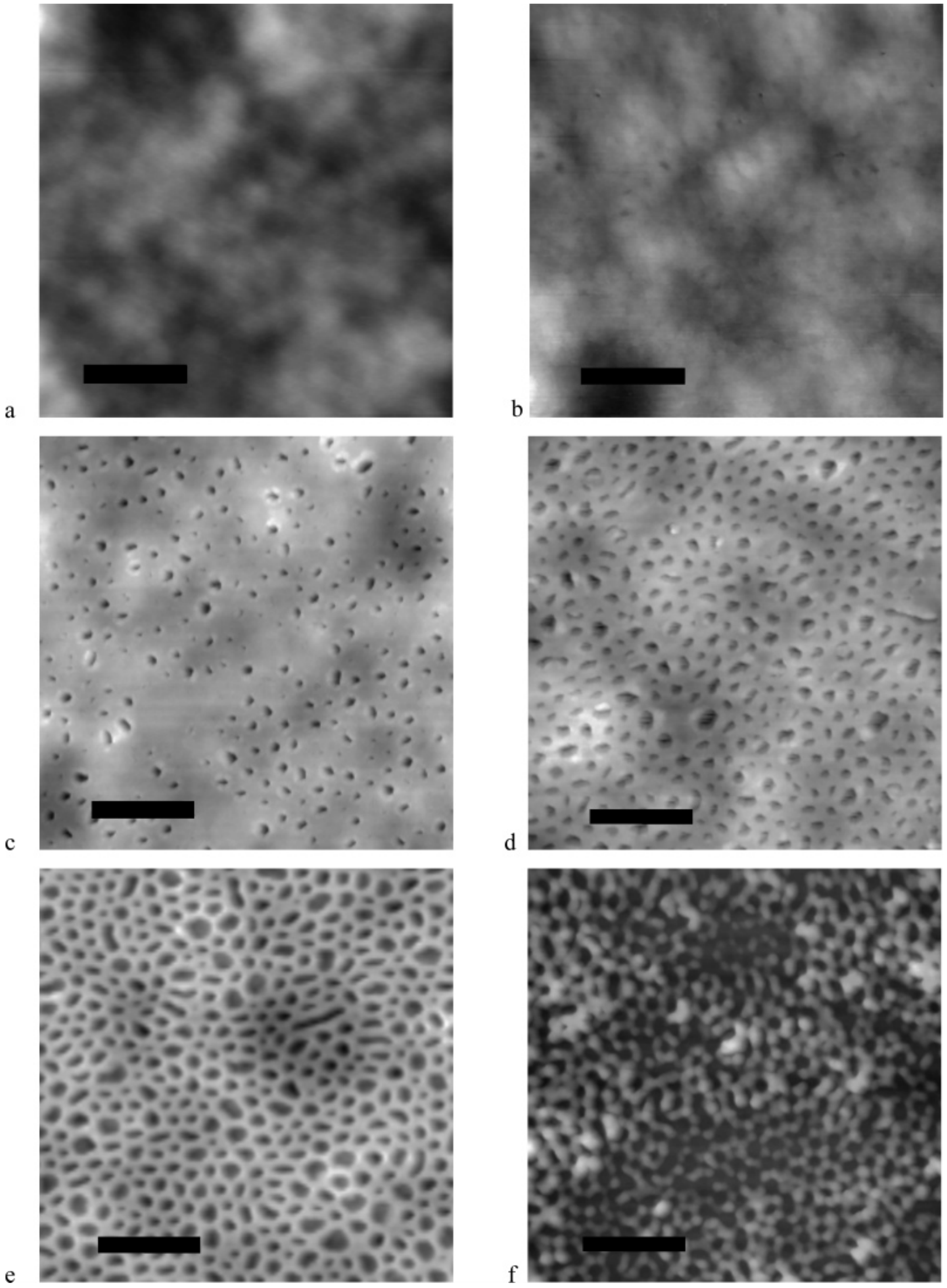

**Figure 2.** Topographic images of PS−PFMA thin films processed with $scCO_2$ at 15 MPa and subsequently etched with an RIE for (a) 0, (b) 10, (c) 13, (d) 15, (e) 20, and (f) 40 s. The bars indicate 200 nm.

that the size estimated by AFM and SEM represented diameter of the cells. While neither AFM nor SEM measures absolute diameters of the cells, the relative dependence can still be well captured.

The number densities of nanocells as functions of saturation pressure and process time are plotted in parts a and b of Figure 4, respectively. As shown in Figure 4a, at 10 MPa pressure, the number density decreases to $8.6 \times 10^{10}$ $cm^{-2}$. The cell structures are not simply templated from the PFMA nanodoamins of as-cast films. Furthermore, the number density decreases rapidly (in 10 min) and then gradually decreases with time, as seen in Figure 4b. $ScCO_2$ annealing is an effective annealing method compared with conventional thermal annealing for strongly interacting and hence slowly relaxing systems.[34,35] $CO_2$ is a good solvent for fluorinated polymers; therefore, $scCO_2$ can penetrate into fluorinated block copolymer, swell the fluorinated blocks significantly relative to the swelling of PS, and reconstruct the nanodomains. It has been reported that the $CO_2$ sorptions in PS are 6.5% and 10.2% at 7.2 MPa (35 °C) and 17.4 MPa (180 °C), respectively.[36,37] $CO_2$ reduces the effective interaction between PS and PFMA and significantly enhances the diffusivity. Therefore, the saturation temperature of 60 °C is well below the $T_g$ of PS (100 °C), but still above the plasticized $T_g$ of PS in $CO_2$. $CO_2$ also changes the effective volume fraction of PFMA domains, i.e., the volume fraction of PFMA plus $CO_2$, since $CO_2$ is selectively localized in PFMA domains. The increasing effective PFMA fraction is likely to drive spherical domains to cylindrical or even to lamellar

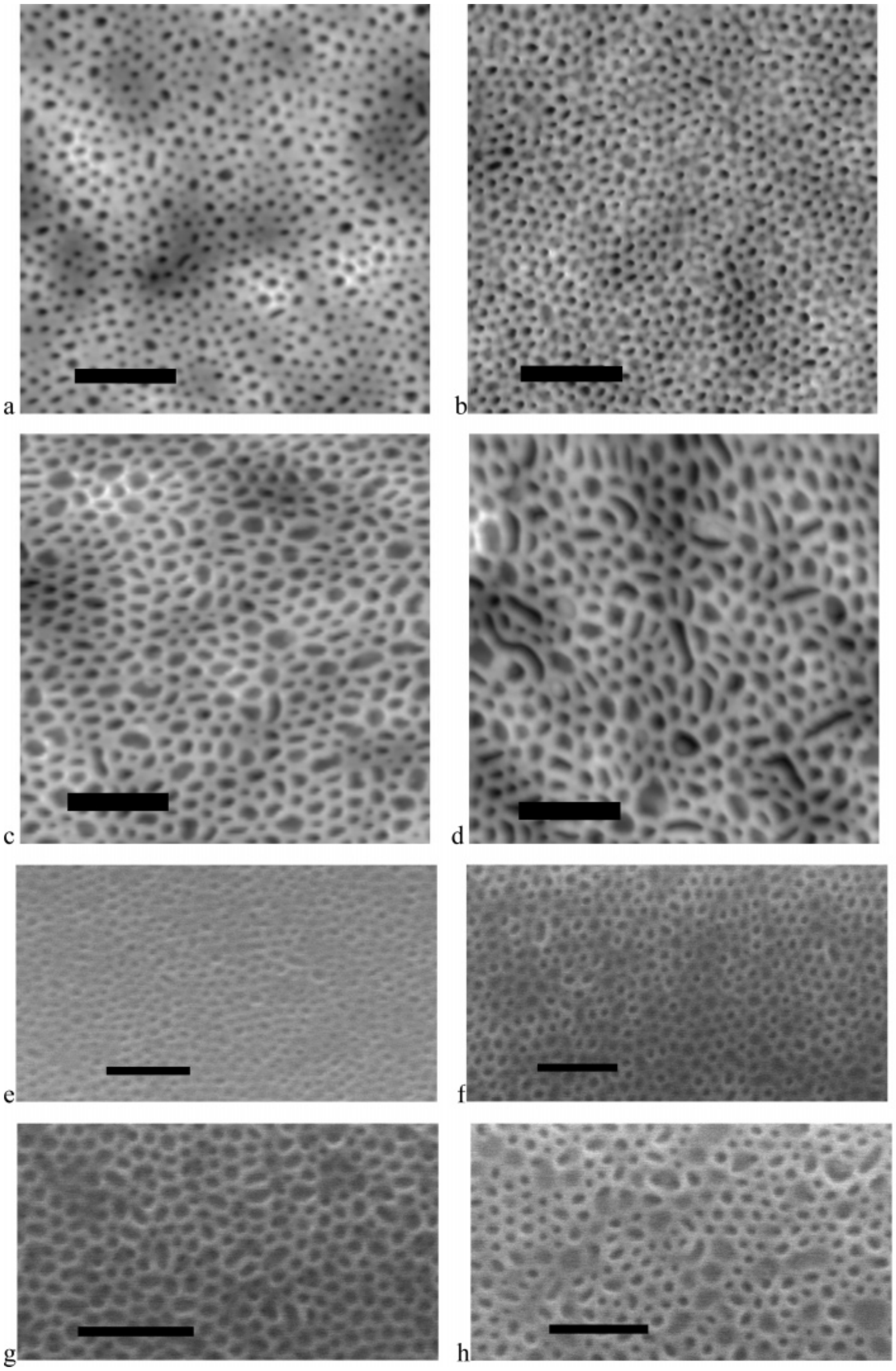

**Figure 3.** Topographic AFM images of nanocellular structures in PS−PFMA47 thin films after the $scCO_2$ process at saturation pressure of 8 MPa with full-scale height of 18 nm (a), 10 MPa with full-scale height of 22 nm (b), 15 MPa with full-scale height of 25 nm (c), and 20 MPa with full-scale height of 27 nm (d). The bars indicate 200 nm. SEM images of the same films processed at 8 (e), 10 (f), 15 (g), and 20 MPa (h). The bars indicate 200 nm.

domains. However, we did not find clear phase transition to cylindrical (channel) structures in our experiments. It is likely that reconstruction of domain shape is still kinetically restricted. In other words, there is a strong influence of initial as-cast morphology, whereas the size and spacing of spherical domains change significantly during the process. Such a system can be a nightmare for understanding and predicting the structures but, conversely, can be advantageous for ultimate control of cellular and porous structures: the structures not available in equilibrium may be accessible. For instance, a honeycomb structure (large volume cells separated by thin separating wall), which cannot be produced by decomposing strategy of particular domains of equilibrium block copolymer morphologies, can be fabricated through this methodology.

The average cell diameter and spacing determined by AFM are plotted in Figure 4c as a function of processing pressures with the bars denoting the standard deviations. The spacing was computed from the first-order peaks (rings) of fast Fourier transformed images. Note that the bars do not represent the experimental errors but primarily the distribution of cell diameter. Both the average cell diameter and the domain spacing increase with increasing saturation pressure. Analytical ellipsometry was used to measure the thicknesses and refractive indices of the films before and after the $CO_2$ process. Since the

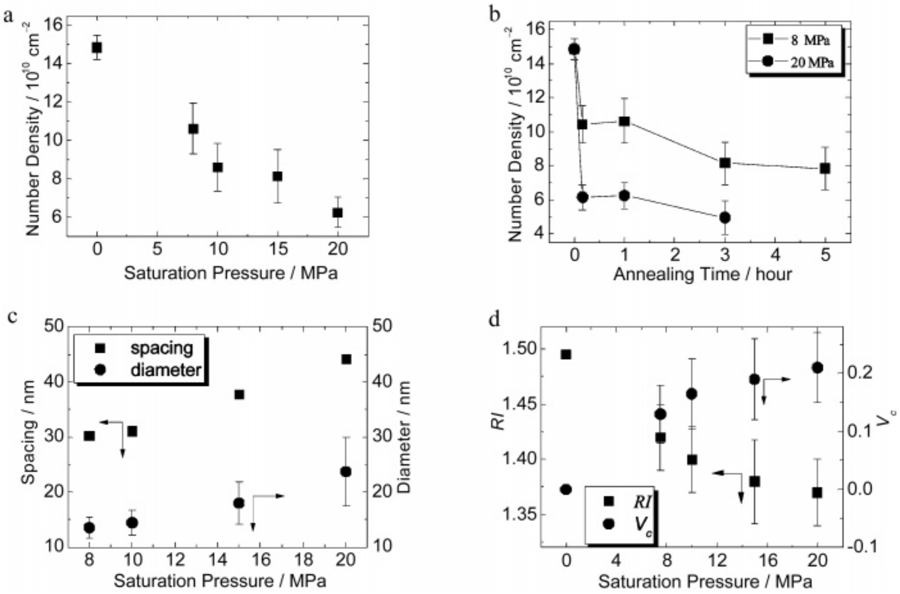

**Figure 4.** (a) Number density of nanocells obtained by AFM against saturation pressures. (b) Saturation time dependence of the number density of nanocellular structures in PS−PFMA thin films at 8 and 20 MPa. (c) Average domain spacing and diameter plotted against $CO_2$ saturation pressures. (d) Dependence on $CO_2$ saturation pressure of refractive index of the films and volume fraction of the introduced voids.

**Table 1. Porosities Estimated by Decrement of Refractive Index ($V_{cn}$) and Increment of Thickness ($V_{ct}$)**

| | *P*/MPa | | | |
|---|---|---|---|---|
| | 8 | 10 | 15 | 20 |
| $V_{cn}$ | 0.13 ± 0.05 | 0.16 ± 0.06 | 0.19 ± 0.07 | 0.21 ± 0.06 |
| $V_{ct}$ | 0.11 ± 0.04 | 0.14 ± 0.03 | 0.18 ± 0.02 | 0.26 ± 0.02 |

size of nanocells is much smaller than wavelength of light, we assume that effective medium approximation is valid. The increments of thicknesses, $\Delta t$, from the original thickness of the film, $t$, after the process with the saturation pressures of 8, 10, 15, and 20 MPa are 5.9, 8.3, 10.2, and 17.3 nm, respectively. The differences in both thickness and refractive index provide two different porosities. A porosity, $V_{cn}$, can be defined from refractive index according to the Lorentz−Lorentz equation[38]

$$\frac{n_f^2 - 1}{n_f^2 + 2} = (1 - V_{cn})\frac{n_s^2 - 1}{n_s^2 + 2} \qquad (1)$$

where $n_f$ and $n_s$ are the refractive indices of a nanocellular film and a solid skeleton, respectively. Another porosity, $V_{ct}$, can also be defined by increment of the thicknesses before and after the process, $V_{ct} = \Delta t/(t + \Delta t)$. $V_{cn}$ and $V_{ct}$ are listed in Table 1, showing a reasonable agreement within the experimental precision. This good agreement indicates conservation of mass during the $CO_2$ process. If copolymer partially dissolved into $CO_2$, $V_{ct}$ would be smaller than $V_{cn}$. The dependences on processing pressure of refractive index and porosity are plotted in Figure 4d. The refractive index decreases to 1.37, equivalent to 22 vol % of porosity, at 20 MPa of saturation pressure. Note that the reduction of refractive index of 47 nm thick films (this study) is not as great as that of 1 $\mu$m thick films (our previous study)[21] while the qualitative trend is the same. The refractive index of a thick film at 20 MPa in our previous study decreases as small as 1.23, i.e. 50% porosity. The reason for this quantitative disagreement is the following: The surface and the silicon interface of PS−PFMA film are covered with the adsorbed layers (a layer of lamella) of the PFMA domains.[39] Such planar layers of PFMA form neither cellular nor porous structure but result in the dense layers at the surface and interface. We have already estimated the surface skin layer is 15 nm by the controlled etching experiment in Figure 2. The schematic pictures of nanocellular thin films containing a single layer and multiple layers of cells are shown in parts a and b of Figure 5, respectively, to demonstrate the influence of the nonfoaming PFMA planner surface and interface layers. Assuming that the silicon interface is covered by a wetting layer of copolymer with a similar thickness (∼15 nm) as that of the surface skin layer, the ratio of the nonfoaming PFMA planar layers (30 nm) is more than 50% of the total original thickness (47 nm) so that the relative contribution of the nonfoaming skin layers at the surface and interface to the overall porosity or refractive index is more significant in thin films than that in 1 $\mu$m thick films.

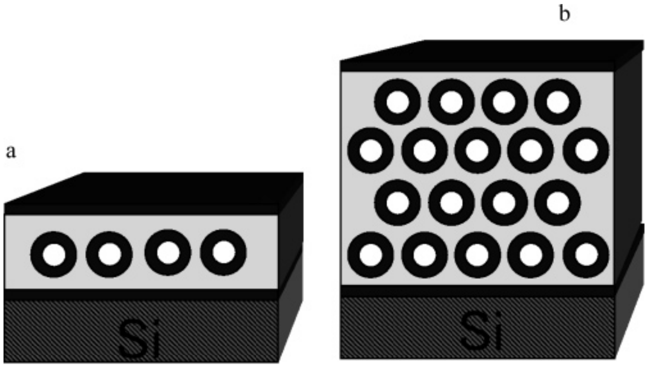

**Figure 5.** Schematic pictures of expected structures in PS−PFMA thin (a) and thick (b) films after the $scCO_2$ process. The voids (white) are surrounded by the PFMA domains (black) and distributed in continuous PS matrix (gray). The surface and interface are covered by PFMA layers.

To observe the cross section of the nanocellular films, we scratched the films at liquid nitrogen temperature and then observed the side wall of the scratch by SEM. Cross sections of PS−PFMA47 processed at 8 and 20 MPa are shown in parts a and b of Figure 6, respectively. Spherical pores are found on the side wall. Assuming a single layer of spheres in such thin

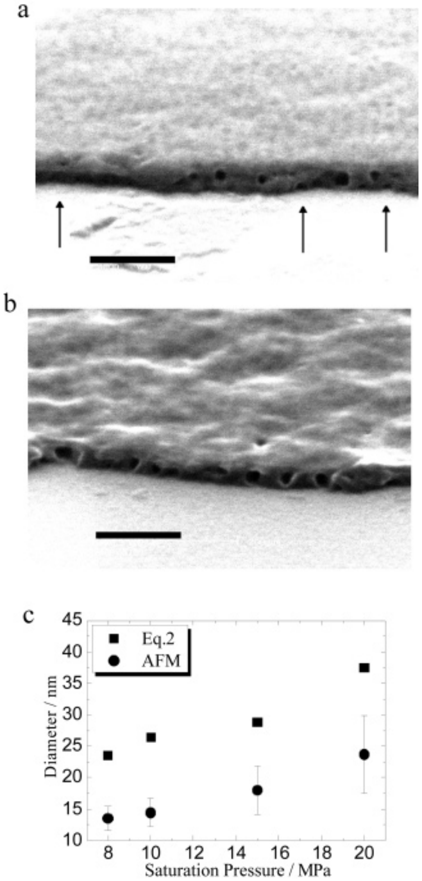

**Figure 6.** Cross-sectional views of PS−PFMA47 thin films at 8 (a) and 20 (b) MPa. The hemispherical cells at the interface in (a) are pointed by arrows. The bars indicate 200 nm. (c) Dependence of diameters of nanocells on saturation pressure in PS−PFMA47 thin films determined by eq 2 and AFM.

film, the following equation determines the average radius, $r$, of nanocells in PS−PFMA thin films.

$$r = [(3\Delta T/(4\pi d)]^{1/3} \tag{2}$$

$\Delta T$ is the increment of film thickness after $scCO_2$ processing, and $d$ is the number density of nanocells determined by in-plane AFM or SEM images. The dependences of cell sizes on the processing pressure determined by eq 2 and AFM are plotted in Figure 6c. The cell size determined by both methods has a similar dependence on saturation pressures. However, the diameter obtained by AFM is smaller than that given by eq 2. This could be caused by occasionally observed hemispherical cells (indicated by arrows in Figure 6a) at the interface with the silicon wafer. Such cells are not observed in the top view after etching of 20−25 nm from the surface; such additional hidden voids overestimate the cell size in eq 2. Cross-sectional SEM images successfully capture such void structures near the substrate interface.

**Multiple Nanocellular Layers in Thin Films.** A PS−PFMA film with a thickness of 140 nm, named PS−PFMA140, was prepared under the same processing conditions as for PS−PFMA47. The selected AFM and SEM images of the top layers and the cross-sectional views of PS−PFMA140 are shown in Figure 7. Reactive ion etching before SEM observation was often necessary to find all the cell structure on the side wall. The top view images using both AFM and SEM reveal that there are closed nanopores similar to PS−PFMA47. Irrespective of film thickness, the top layer structures are the same: spherical cellular structure is always observed, and the number densities of the cells are equivalent. No evidence of connectivity is found in either cross section or surface. Single and multiple layers of cells have almost indistinguishable structures in the topmost layers except in the films processed at a high $CO_2$ saturation pressure. We will discuss this issue later in this section. Even in monolithic specimens,[21] the apparent size of cells is almost the same for the specimens processed with the same conditions. This fact indicates there is a negligible confinement effect of a substrate for the nanocellular formation. Evidently, decreasing number densities after the $CO_2$ process shown in Figure 4a,b suggests that the original spherical domain structure is not the simple template for the cellular structure. If $CO_2$ simply swells the spherical domain structure isotropically without changing aggregation number, the dimension of the film does not match the size of the silicon substrate. If the spherical domains are fixed in the $xy$ plane (the surface plane of the substrate) and the film swells only in the $z$ direction, the number density of nanocells in the top views should remain unchanged. Conversely the number density decreases as a function of time and pressure, whereas the total amount of copolymer on the substrate is conserved. Additionally, the cross-sectional views of the nanocellular films show spherical cells which are not elongated in the $z$ direction. Therefore, when the films are swollen with $CO_2$, the aggregation number (number density) changes by diffusion of block copolymer chains so that the confinement effect of substrate is reduced. However, it should be noted that structural reconstruction, i.e., spheres to cylinders or lamellae, was not observed in our system despite that PFMA domains were selectively swollen.

While we find negligible difference between the thin monolayer of cells and thick multiple layers of cells at low saturation pressures, the difference becomes visible as $CO_2$ saturation pressure increases to 20 MPa. The distributions of apparent diameter estimated from AFM images are plotted in Figure 8. Irrespective of the thickness, the diameters increase with saturation pressure. However, a small number of significantly larger cells appear at elevated pressures. Such larger cells may be formed by coalescence of small cells by popping up the wall separating the neighboring cells. A similar bimodal distribution is also observed in thick cellular monoliths in our previous study.[40] Such a coalescence process of nanocells should be more visible in reduced dimension. In 2 dimensions, i.e. a single layer of cells, coalescence occurs only in the $xy$ plane (substrate plane). Therefore, the coalescence is always observed in an $xy$ plane view. However, thick multiple layers permit coalescence in all three dimensions, and hence the coalescence in the $z$-direction cannot be observed in the $xy$ plane view. In the histogram, the fraction of larger cells appear to be greater in the single layer film than that in the multiple layered film.

**Obtaining Monodispersed Nanocells.** The key step of fabricating nanocells in fluorinated copolymer thin films and monoliths is quenching temperature to 0 °C to freeze the PS matrix so that the fixed nanocellular structures are preserved during the depressurization process. As discussed in our previous work (ref 40), depressurization temperature ($T_d$) has a significant influence on the size of cells in bulk. Nanoscale cells can be obtained only when $T_d$ is lower than glass transition temperature, $T_g$, of the matrix; otherwise, both micro- and nanoscale cells will be formed. When we skipped the saturation process at 60 °C and pressurized a PS−PFMA film at 0 °C (the $T_g$ of PS swollen by $scCO_2$ is as low as 30 °C),[41] the film did not change the thickness, indicating no nanocellular formation. Therefore, morphological change during temperature quench is not con-

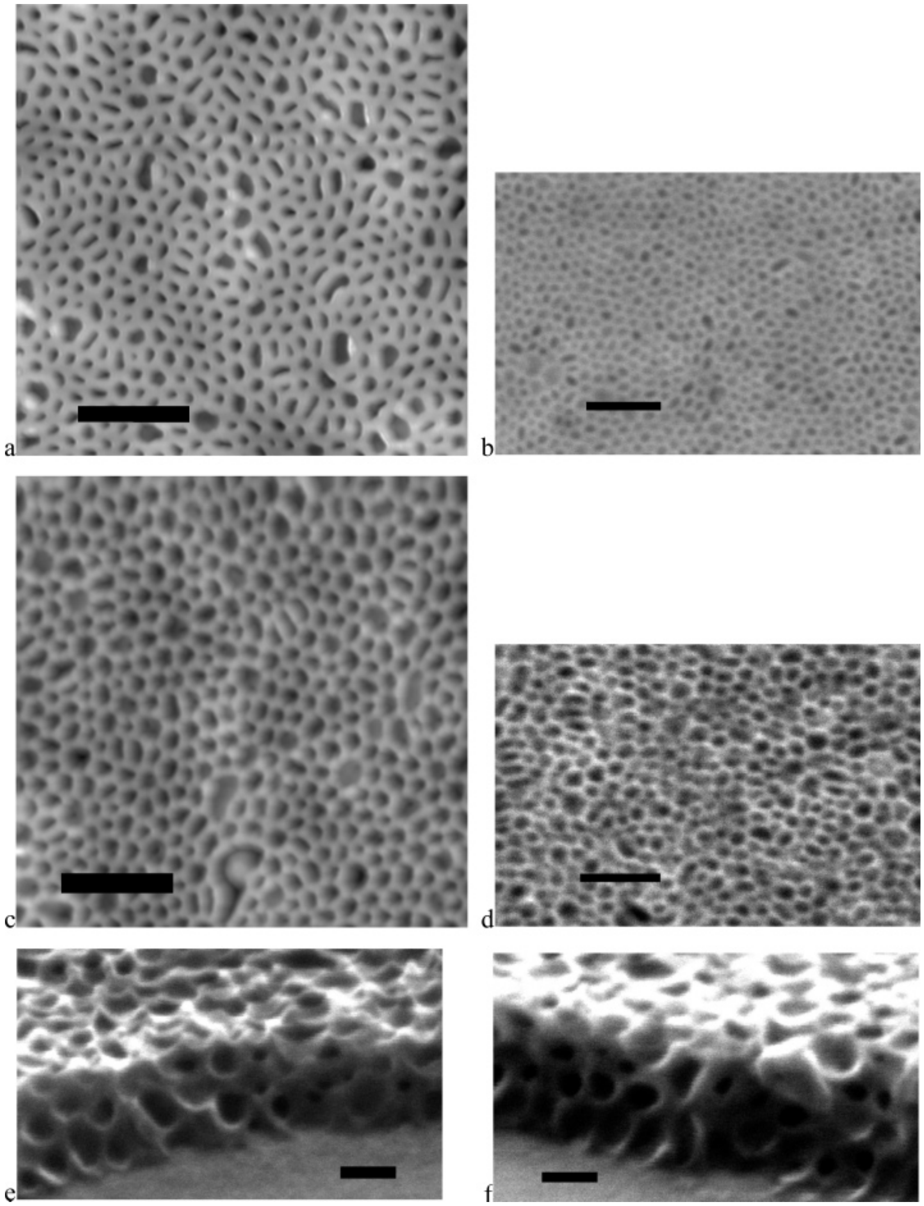

**Figure 7.** Topographic (a) and SEM (b) images of nanocellular structures in PS−PFMA140 after the $scCO_2$ process at a saturation pressure of 10 MPa and etching. Topographic (c) and SEM (d) images of nanocellular structures in PS−PFMA140 after the $scCO_2$ process at a saturation pressure of 20 MPa and etching. The bars indicate 200 nm. Cross-sectional views of PS−PFMA140 processed at 10 (e) and 20 (f) MPa. The bars indicate 50 nm.

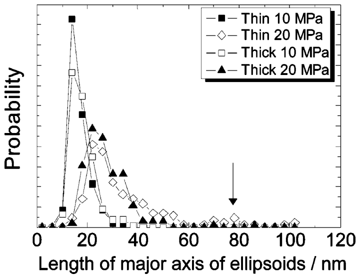

**Figure 8.** A histogram of size distributions of nanocells in thin (47 nm) and thick (140 nm) films processed at 10 and 20 MPa of $CO_2$. The length of major axis was measured in the case of ellipsoidal cells. The arrow indicates the presence of larger cells at elevated saturation pressure.

trolled by the affinity of PFMA block to $CO_2$ but by the mobility of PS in $CO_2$. Soaking and quenching processes are both important for nanocellular formation. As shown in Figure 4c, both the size and distribution of nanocells in copolymer thin films increase with increasing saturation pressure, which is the consequence of decreasing $T_g$ of the PS matrix with pressure and increasing solubility of PFMA in $CO_2$. While cooling specimens to 0 °C preserves the structure, we still find some size distribution in the final nanocellular films, especially at elevated pressures. Although the $T_g$ of PS swollen by $scCO_2$ is 30 °C or above,[41] the saturation pressure (degree of plasticization) may still influence the modulus of the PS domains at 0 °C. By further reducing the depressurization temperature, $T_d$, to −40 °C, far below the $T_g$ of PS in $CO_2$, the PS matrix becomes more rigid and possibly keeps the cell structure from expanding and coalescing. The histograms of cell size at different $T_d$ are shown in Figure 9 to demonstrate the effects of lowering $T_d$ on the size distribution. The film depressurized at −40 °C displays the size distribution that is much narrower than that depressurized at 0 °C. The improved regularity at −40 °C and slightly smaller cell diameter clearly indicate that the cells expand in some degree upon depressurization even at 0 °C. If the affinity of PFMA to $CO_2$ governs the process, reducing temperature increases the affinity, swells copolymer further, and

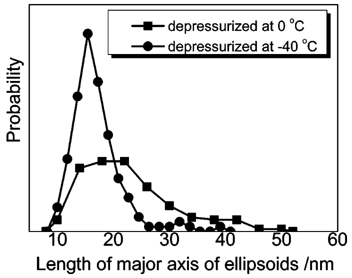

**Figure 9.** Histogram of size distribution of nanocells processed at 15 MPa pressure and depressurizated at 0 and −40 °C.

produces larger cells. We speculate that the size of the cells depressurized at −40 °C is solely determined by the swelling of PFMA domains. While the solubility of PFMA in $CO_2$ is significantly enhanced at reduced temperature, the size of cells is rather reduced. This fact indicates that the nanocellular process is strongly influenced by the mobility of skeleton domains (PS in this case) in the presence of $CO_2$. Consequently, the cellular formation is a combination of swelling and expansion of PFMA domains by $CO_2$.

Assuming that the uniform cells expand upon depressurization, another strategy of reducing the size distribution is making the wall separating the cell thicker and preventing the expansion of the cells: this modification can be achieved by adding a low molecular weight PS to the block copolymers.[42,43] It has been known that the added PS is partitioned in the PS domains of the block copolymer without macroscopic phase separation provided that the molecular weight of the PS is lower than the molecular weight of the copolymer. The effect of adding low molecular weight homopolymer on the size and spacing of nanocells was investigated by mixing 35% weight ratio homo-PS (weight-average molecular weight 4700 with a polydispersity index 1.07, Polymer Source Inc.) with PS−PFMA. The average PFMA weight fraction was reduced to 26%. No macrophase separation is observed in the as-cast films; only spherical PFMA domains are found with a density $7.4 \times 10^{10}$ cm$^{-2}$ and spacing 37.3 nm. Compared with the PS−PFMA as-cast film, the density of PFMA nanodomains decreases, while the spacing increases slightly. After the $scCO_2$ process at 20 MPa, the refractive index decreases from 1.55 to 1.45, indicating 15.6 vol % of voids are introduced into thin film. The AFM picture of the resultant nanocells is shown in Figure 10a. The density and spacing of these nanocells are $3.9 \times 10^{10}$ cm$^{-2}$ and 41.8 nm, respectively. The histograms of diameter is shown in Figure 10b, providing the average diameter of 15.0 nm and standard deviation of 2.4 nm. The size of cells in this mixture is monodispersed and similar to that in Figure 9, in which the film was depressurized at −40 °C. The thicker walls separating the cells also prevent the cells from expanding upon depressurization and provide a uniform cell distribution. Both lowering the depressurization temperature and adding low molecular weight homopolymer are proved to be effective methods to control the size distribution of nanocells. In addition, such experiments suggest that the cell size is primarily determined by the volume of $CO_2$ trapped in the PFMA domains, but such cells expand depending on the depressurization temperature.

## Conclusion

Nanocellular formation of $CO_2$ in PS−PFMA block copolymer thin films has been comprehensively studied. We have found closed cellular structures in single layered films as well as multiple layered films. The closed cell structures have been confirmed by in-plane and cross-sectional views of the films. Number density of cells in the in-plane view is always smaller than that of PFMA domains before the $CO_2$ process; therefore, the cells are not simply templated from the PFMA domains. Structure reconstruction is evident during the $CO_2$ process. However, reconstruction of cell (pore) shape, e.g. spheres to cylinders, was not observed although the PFMA fraction of the copolymer was more than 29 vol %. The influence of initial morphology is not negligible. The size and density of nanocells are controlled primarily by saturation pressure. In addition, reducing depressurization temperature and adding low molecular weight homopolymer also reduce the size of cells and the size distribution. Expansion of cells is not negligible even at 0 °C, which is 30 °C below the $T_g$ of skeleton PS in the presence of $CO_2$. Reducing the depressurization temperature down to −40 °C effectively prevents the expansion, and the nanocells with uniform size are obtained. The same effect is found by adding a low molecular weight PS into the PS−PFMA copolymer and hence making the wall separating the cells thicker.

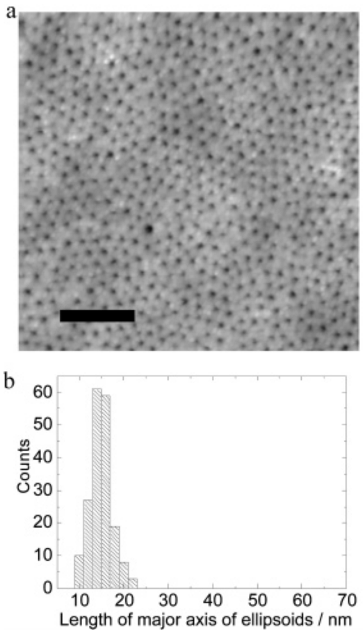

**Figure 10.** (a) A topographic image of nanocellular structures in a PS−PFMA thin film with adding 35% low molecular weight homo-PS after the $scCO_2$ process at a pressure of 20 MPa and etching. (b) Histogram of nanocells size distribution in PS−PFMA thin film with adding homo-PS after the $scCO_2$ process at 20 MPa.

**Acknowledgment.** This research was partially funded by the Project on Nanostructured Polymeric Materials of New Energy and Industrial Technology Development Organization. We thank the Japan Society for the Promotion of Science for the funding and fellowship.

## References and Notes

(1) Lee, S. B.; Mitchell, D. T.; Trofin, L.; Nevanen, T. K.; Soederlund, H.; Martin, C. R. *Science* **2002**, *296*, 2198−2200.
(2) Kohli, P.; Harrell, C. C.; Cao, Z. H.; Gasparac, R.; Tan, W. H.; Martin, C. R. *Science* **2004**, *305*, 984−986.
(3) Linssen, T.; Cassiers, K.; Cool, P.; Vansant, E. F. *Adv. Colloid Interface Sci.* **2003**, *103*, 121−147.
(4) Lazzeri, P.; Vanzetti, L.; Anderle, M.; Bersani, M.; Park, J. J.; Lin, Z.; Briber, R. M.; Rubloff, G. W.; Kim, H. C.; Miller, R. D. *J. Vac. Sci. Technol. B* **2005**, *23*, 908−917.
(5) Lazzari, M.; Lopez-Quintela, M. A. *Adv. Mater.* **2003**, *15*, 1583−1594.
(6) Park, C.; Yoon, J. S.; Thomas, E. L. *Polymer* **2003**, *44*, 6725−6760.
(7) Lee, J. S.; Hirao, A.; Nakahama, S. *Macromolecules* **1988**, *21*, 276−278.

(8) Lee, J. S.; Hirao, A.; Nakahama, S. *Macromolecules* **1989**, *22*, 2602−2606.

(9) Zalusky, A. S.; Olayo-Valles, R.; Wolf, J. H.; Hillmyer, M. A. *J. Am. Chem. Soc.* **2002**, *124*, 12761−12773.

(10) Thurn-Albrecht, T.; Steiner, R.; DeRouchey, J.; Stafford, C. M.; Huang, E.; Bal, M.; Tuominen, M.; Hawker, C. J.; Russell, T. P. *Adv. Mater.* **2000**, *12*, 781−791.

(11) Chan, V. Z. H.; Hoffman, J.; Lee, V. Y.; Iatrou, H.; Avgeropolulos, A.; Hadjichristidis, N.; Miller, R. D.; Thomas, E. L. *Science* **1999**, *286*, 1716−1719.

(12) Liu, G. J.; Ding, J. F.; Guo, A.; Herfort, M.; Bazett-Jones, D. *Macromolecules* **1997**, *30*, 1851−1853.

(13) Liu, G. J.; Ding, J. F.; Stewart, S. *Angew. Chem., Int. Ed.* **1999**, *38*, 835−838.

(14) Hashimoto, T.; Tsutsumi, K.; Funaki, Y. *Langmuir* **1997**, *13*, 6869−6872.

(15) Thurn-Albrecht, T.; Schotter, J.; Kastle, C. A.; Emley, N.; Shibauchi, T.; Krusin-Elbaum, L.; Guarini, K.; Black, C. T.; Tuominen, M. T.; Russell, T. P. *Science* **2000**, *290*, 2126−2129.

(16) (a) DeSimone, J. M.; Guan, Z.; Elsbernd, C. S. *Science* **1992**, *257*, 945−947. (b) Romack, T. J.; Maury, E. E.; DeSimone, J. M. *Macromolecules* **1995**, *28*, 912−915. (c) Svec, F.; Freachet, J. M. J. *Ind. Eng. Chem. Res.* **1998**, *38*, 34−38. (d) Cooper, A. I.; Holmes, A. B. *Adv. Mater.* **1999**, *11*, 1270−1274. (e) Watkins, J. J.; McCarthy, T. J. *Macromolecules* **1994**, *27*, 4845−4847. (f) Loy, D. A.; Russick, E. M.; Yamanaka, S. A.; Baugher, B. M.; Shea, K. J. *Chem. Mater.* **1997**, *9*, 2264−2268. (g) Chester, T. L.; Pinkston, J. D.; Raynie, D. E. *Anal. Chem.* **1998**, *70*, 301−320. (h) Siripurapu, S.; DeSimone, J. M.; Khan, S. A.; Spontak, R. J. *Macromolecules* **2005**, *38*, 2271−2280. (i) Siripurapu, S.; Coughlan, J. A.; Spontak, R. J.; Khan, S. A. *Macromolecules* **2004**, *37*, 9872−9879. (j) Siripurapu, S.; DeSimone, J. M.; Khan, S. A.; Spontak, R. J. *Adv. Mater.* **2004**, *16*, 989−994.

(17) Lin, Q. H.; Pearson, R. A.; Hedrick, J. C. *ACS Symp. Ser.* **2004**, *874*, 223−235.

(18) Krause, B.; Diekmann, K.; van der Vegt, N. F. A.; Wessling, M. *Macromolecules* **2002**, *35*, 1738−1745.

(19) Cooper, A. I. *Adv. Mater.* **2003**, *15*, 1049−1059.

(20) Hanrahan, J. P.; Copley, M. P.; Ryan, K. M.; Spalding, T. R.; Morris, M. A.; Holmes, J. D. *Chem. Mater.* **2004**, *16*, 424−427.

(21) Yokoyama, H.; Li, L.; Nemoto, T.; Sugiyama, K. *Adv. Mater.* **2004**, *16*, 1542−1546.

(22) Li, L.; Yokoyama, H.; Nemoto, T.; Sugiyama, K. *Adv. Mater.* **2004**, *16*, 1226−1229.

(23) Sugiyama, K.; Nemoto, T.; Koide, G.; Hirao, A. *Macromol. Symp.* **2002**, *181*, 135−153.

(24) Winters, H. F.; Coburm, J. W.; Kay, E. *J. Appl. Phys.* **1977**, *48*, 4973−4812.

(25) Hall, T. M.; Wagner, A.; Thompson, L. F. *J. Appl. Phys.* **1982**, *53*, 3997−4010.

(26) Yokoyama, H.; Kramer, E. J. *Macromolecules* **1998**, *31*, 7871−7876.

(27) Yokoyama, H.; Kramer, E. J.; Rafailovich, M. H.; Sokolov, J.; Schwarz, S. A. *Macromolecules* **1998**, *31*, 8826−8830.

(28) Cavicchi, K. A.; Lodge, T. P. *J. Polym. Sci., Part B: Polym. Phys.* **2003**, *41*, 715−724.

(29) Yokoyama, H.; Mates, T. E.; Kramer, E. J. *Macromolecules* **2000**, *33*, 1888−1898.

(30) Magerle, R. *Phys. Rev. Lett.* **2000**, *85*, 2749−2752.

(31) Hirao, A.; Koide, G.; Sugiyama, K. *Macromolecules* **2002**, *35*, 7642−7651.

(32) Yokoyama, H.; Tanaka, K.; Takahara, A.; Kajiyama, T.; Sugiyama, K.; Hirao, A. *Macromolecules* **2004**, *37*, 939−945.

(33) Yokoyama, H.; Sugiyama, K. *Langmuir* **2004**, *20*, 10001−10006.

(34) Hu, X. C.; Gido, S. P.; Russell, T. P.; Iatrou, H.; Hadjichristidis, N.; Abuzaina, F. M.; Garetz, B. A. *Macromolecules* **2005**, *38*, 4719−4728.

(35) RamachandraRao, V. S.; Gupta, R. R.; Russell, T. P.; Watkins, J. J. *Macromolecules* **2001**, *34*, 7923−7925.

(36) Wissinger, R. G.; Paulaitis, M. E. *J. Polym. Sci., Phys. Ed.* **1987**, *25*, 2497−2510.

(37) Sato, Y.; Yurugi, M.; Fujiwara, K.; Takishima, S.; Masuoka, H. *Fluid Phase Equilib.* **1996**, *125*, 129−138.

(38) Born, M.; Wolf, E. In *Principles of Optics*; Cambridge University Press: Cambridge, UK, 1999.

(39) The adsorption of PFMA to the silicon surface is apparently due to the small fraction of polar groups such as −COOH of the imperfect fluoromethacrylate.

(40) Yokoyama, H.; Sugiyama, K. *Macromolecules* **2005**, *38*, 10516−10522.

(41) Wang, W. C. V.; Kramer, E. J.; Sachse, W. H. *J. Polym. Sci., Polym. Phys. Ed.* **1982**, *20*, 1371−1384.

(42) Tanaka, H.; Hasegawa, H.; Hashimoto, T. *Macromolecules* **1991**, *24*, 240−251.

(43) Jeong, U.; Ryu, D. Y.; Kho, D. H.; Lee, D. H.; Kim, J. K.; Russell, T. P. *Macromolecules* **2003**, *36*, 3626−3634.

MA060325L